MDPI

Article

Characteristics of Yellow Sea Fog under the Influence of Eastern China Aerosol Plumes

Jiakun Liang and Jennifer D. Small Griswold *

Atmospheric Sciences Department, University of Hawaii at Mānoa, 2525 Correa Rd., Honolulu, HI 96822, USA; jiakun@hawaii.edu
* Correspondence: smalljen@hawaii.edu

Abstract: Sea fog is a societally relevant phenomenon that occurs under the influence of specific oceanic and atmospheric conditions including aerosol conditions. The Yellow Sea region in China regularly experiences sea fog events, of varying intensity, that impact coastal regions and maritime activities. The occurrence and structure of fog are impacted by the concentration of aerosols in the air where the fog forms. Along with industrial development, air pollution has become a serious environmental problem in Northeastern China. These higher pollution levels are confirmed by various satellite remote sensing instruments including the Moderate Resolution Imaging Spectroradiometer (MODIS) aboard the Aqua satellite that observes aerosol and cloud properties. These observations show a clear influence of aerosol loading over the Yellow Sea region, which can impact regional sea fog. In this study, high-resolution data sets from MODIS Aqua L2 are used to investigate the relationships between cloud properties and aerosol features. Using a bi-variate comparison method, we find that, for most cases, larger values of COT (cloud optical thickness) are related to both a smaller DER (droplet effective radius) and higher CTH (cloud top height). However, in the cases where fog is thinner with many zero values in CTH, the larger COT is related to both a smaller DER and CTH. For fog cases where the aerosol type is dominated by smoke (e.g., confirmed fire activities in the East China Plain), the semi-direct effect is indicated and may play a role in determining fog structure such that a smaller DER corresponds with thinner fog and smaller COT values.

Keywords: Yellow Sea fog; aerosol; MODIS Aqua; aerosol–cloud interactions

1. Introduction

Fog is defined as water droplets suspended in the atmosphere near the surface of the earth that can reduce visibility below 1 km. Sea fog usually refers to the fog that occurs under the influence of the ocean [1]. It is a global phenomenon that occurs in coastal regions and over the open ocean, especially in the Northwest Atlantic and Pacific regions [2]. With the expansion and development of air, land, and sea traffic, sea fog has the potential to have a significant impact on human activities. It can influence marine transportation, harbor activities, coastal road traffic, and other maritime activities [3]. Economic losses caused by low visibility due to sea fog can be comparable to those caused by other weather events such as tornadoes, or even hurricanes [4,5].

Yellow Sea fog usually occurs on the coast of the Shandong Peninsula [3]. Stations along the northwest Yellow Sea coast normally record more than 50 foggy days annually, while Chengshantou (CST) station in the northern Yellow Sea records a maximum of over 80 days of fog [6]. Previous studies characterize Yellow Sea fog as cold advection fog, which refers to the type of fog that is generated when warm, moist air moves over the colder sea surface [2,7]. Yellow Sea fog forms when the prevailing south-southeast (SSE) winds bring moist air above the warm branch of the Kuroshio Current under synoptic and hydrologic conditions that are conducive to sea fog formation [6,8]. The sea surface temperature (SST) also plays an important part in the formation and maintenance mechanism of sea fog. The

colder shelf regions caused by tidal mixing can result in a higher frequency of sea fog along the Korean coast of the Yellow Sea and a longer fog season [3,6,9,10].

In general, the Yellow Sea's fog season begins in April with the occurrence of the basin-scale anticyclone over the Yellow Sea and northern East China Seas and ends in August under the influence of the large-scale shift in the East Asian summer monsoons [6]. Additionally, the Yellow Sea fog season can be further divided into spring (from April to May) and summer (July) fogs based on differences in formation mechanisms and occurrence frequency [11]. The temperature difference between the land and sea leads to the formation of a shallow anticyclone over the cooler Yellow Sea in April, and the southerly winds on the west of this anticyclone can transport the warm and moist air from the south to the cold Yellow Sea and cause the abrupt beginning of spring Yellow Sea fog. The summer Yellow Sea fog is related to the East Asian-Western Pacific monsoons, which change the prevailing wind direction from southerly to easterly [6,11]. With the process of global warming, the frequency of sea fog in the midlatitude of the Northwestern Pacific is decreasing due to the westward extending and southward shifting of the subtropical high with reduced northward moisture transportation [12].

Additionally, anthropogenic activities alter the atmospheric composition via aerosols which can impact fog development and characteristics. Atmospheric particulate matter has a major impact on the global climate, and it can affect the atmosphere in both direct and indirect ways [13]. Aerosols can change the radiative balance of the earth–atmosphere system directly and influence the atmosphere indirectly by changing the properties, amount, and lifetime of clouds by modifying cloud microphysical processes [14–18]. Especially, the changes in the humidity and stability of the troposphere caused by the semi-direct effect can lead to changes in the formation and lifetime of clouds [19]. Certain aerosol types, e.g., smoke, absorb sunlight and increase the air temperature relative to the temperature of the surface when the boundary layer becomes filled with dark-colored particles, and this heating at the top of the boundary layer can burn away (evaporate) clouds [19,20].

The meteorological conditions that favor the sea fog process also favor the accumulation of aerosols and pollutants [21]. Both fog and aerosols occur most commonly in the planetary boundary layer [22]. Previous studies have shown how aerosols influence fog properties and what role aerosols play during fog episodes [21,23–25]. Aerosol size plays a more important role when they are acting as CCNs (cloud condensation nuclei) than the chemistry of the aerosol; however, these physical features can change during fog episodes [25,26].

Due to large fossil fuel consumption and anthropogenic activities related to industrial emissions and heavy traffic, North China suffers from air pollution [27]. As a result, sulfate and nitrate are the main secondary aerosol particles in Northern and Eastern China [28,29]. The precursors of SO_2, NO_x, and NH_3 can substantially influence the formation and microphysics of fog [30]. As an essential proportion of atmospheric aerosols in the troposphere, secondary organic aerosols (SOAs) can impact the environment and human health, and can be related to fog events [31]. Higher concentrations of SOAs are observed during fog episodes compared with clear days [32]. In contrast to the climate cooling provided by the reflection of sunlight from low clouds, smoke can warm the atmosphere. Smoke can stabilize the temperature profile of the atmosphere by warming the free troposphere and cooling the surface below, which enhances the low cloud deck, resulting in improved cooling from the some-plus-cloud effect [33].

This study aims to identify sea fog cases between 2002 and 2020 and investigate the relationship between aerosols and cloud properties. Using the high-resolution data from MODIS Aqua L2, we conducted a bi-variate comparison to study the relationship between COT, CTH, and DER for 15 selected Yellow Sea fog cases.

2. Data

Datasets from the surface observation stations are used to identify sea fog cases. Satellite observations of aerosol and cloud properties from MODIS aboard the Aqua satellite (http://modis.gsfc.nasa.gov/, accessed on 5 March 2023) over the Yellow Sea are used to study the identified sea fog events under different aerosol conditions. Satellite Aqua was launched on 4 May 2002; it passes from north to south across the equator in the afternoon (at approximately 1330 Local Standard Time (LST)) and views the entire surface of the earth every 2 days [34]. The research period from 2002 to 2020 is investigated here in order to be consistent with satellite data, and only days in the fog season (from April to August) are selected. Reanalysis data from the National Centers for Environmental Prediction (NCEP) and the National Center for Atmospheric Research (NCAR) (https://psl.noaa.gov/, accessed on 2 April 2023) are used to study temperature advection around the Yellow Sea area.

2.1. Surface Station Data

Surface station observations, recorded every 3 h, from the NCEI (NOAA National Centers for Environmental Information, https://www.ncei.noaa.gov/, accessed on 27 May 2023), are used to identify Yellow Sea fog cases. In the current work, six surface stations near Qingdao are used to study the sea fog occurrence: QD (Qingdao), CST (Chengshantou), LY (Laiyang), LT (Liuting), QLI (Qianli Island), and SD (Shidao). Due to insufficient data availability for the research period (2002–2020), the CST station, with its comprehensive dataset spanning from 1973 to 2020, is utilized to identify fog cases, in conjunction with other stations to ensure consistency. Bari [35] showed that fog is indicated when visibility is documented to be less than 1 km. A fog day can be defined as when fog is observed at least once in 24 h [3]. Historically, there have been 534 cases from 1946 to 2020 with visibility of less than 1 km. Of the 534 cases, 217 cases occured within our research period. However, fog may not be the only factor that causes visibility of less than 1 km due to unavoidable instrument errors. Therefore, other methods are needed to verify the remaining cases.

2.2. Satellite Data

Datasets from MODIS used in this study include: (1) MODIS L1B Granule Images, (2) MODIS Aqua high-resolution Level 2 data, and (3) SST data (from GHRSST).

Satellite images from MODIS are used to confirm the fog days from the 217 cases identified with observation data from the CST station. Only cases where the entire fog area is observed by MODIS are included. Figure 1 shows example satellite images of different fog cases from MODIS Granule RGB Images to demonstrate the selection process. The fog area on 3 May 2020 (Figure 1a) shows an unselected case where the fog area is not fully visible and is in the corner of the satellite image. For the second fog example on 31 July 2020 (Figure 1b), the fog over the Yellow Sea is almost covered by high clouds and cannot be seen, so it is also rejected. These two cases cannot provide a clear view of the complete fog area, compared with the fog case on 28 March 2012 (Figure 1c). After careful selection, 15 cases are chosen for this research, and 4 of them (2 May 2008; 3 May 2009; 4 May 2009; 28 March 2012) were confirmed by former studies [11,36–38].

High-resolution datasets from MODIS Aqua L2 are used to investigate the relationships between cloud properties, aerosols, and SST features. The specific cloud properties used here are AOD (aerosol optical depth, 10×10 km, [39]), DER (1×1 km, [40]), COT (1×1 km, [40]), CTT (cloud top temperature, 5×5 km, [40]), and CTH (5×5 km, [40]). As a supplement, the land-sea mask (1×1 km, [39]) is used here to focus on the sea fog over the ocean area.

High-resolution sea surface temperature (SST, 1×1 km) data from GHRSST (https://www.ghrsst.org, accessed on 28 May 2023) are used to study the influence of underlying surface heating. The GHRSST is an open international science group that promotes the application of satellites for monitoring SST. The GHRSST data product used in this study is based on MODIS Aqua. Verification of the MODIS Aqua SST products by

using buoy data in the coastal waters of the Yellow Sea has shown that MODIS SST agreed well with buoy observations, though the accuracy for spring and summer is lower than that for autumn and winter because of the sea fog along the Shandong peninsula [41].
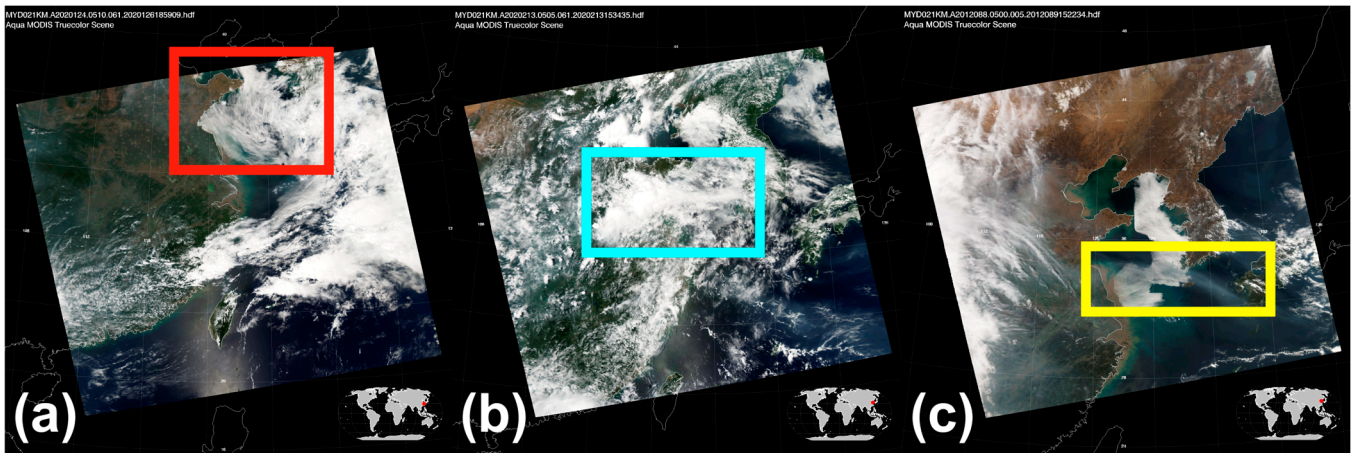

Figure 1. MODIS Aqua L1B Granule Images highlighting different fog case scenarios. (**a**) Fog case on 2 May 2020, red box: "incomplete" fog area, the upper portion of the Yellow Sea is not included in the MODIS granule. (**b**) Fog case on 31 July 2020, cyan box: fog area covered by high cloud. (**c**) Fog case on 28 March 2012, yellow box: pollution (aerosol) band visible on and offshore.

2.3. Soundings

In this study, sounding files at 0000 Coordinated Universal Time (UTC) from the website of the University of Wyoming [42] (http://weather.uwyo.edu/upperair/sounding.html, accessed on 1 June 2023) are used. Here, the dewpoint temperature and air temperature of QD soundings are used to study the fog vertical structures over the northwestern Yellow Sea and identify the height of temperature inversions.

2.4. Reanalysis Data

When analyzing the synoptic conditions of sea fog cases, wind and air temperature data sets are used to calculate the temperature advection. The daily wind and air temperature data are from the NCEP/NCAR reanalysis dataset at multiple pressure levels, with a resolution of $2.5° \times 2.5°$ on global grids.

3. Methods

3.1. CTH Modification

The current CTH retrieval algorithms do not suit stratocumulus clouds, such that errors occur when identifying CTH under strong temperature inversions in the boundary layer using the MODIS satellite, especially for marine stratocumulus clouds [43,44]. This disparity is demonstrated by comparing the MODIS CTH with the CTH values from the geometric methods utilized by the Multiangle Imaging Spectroradiometer (MISR) on the same satellite platform and in situ observations, and this disparity can lead to a CTH inaccuracy of around 2 km [45].

Determining CTH for low-level clouds under strong inversions requires additional information, such as the assumption of the temperature lapse rate from below the cloud top to the surface, 11 μm brightness temperature, and the surface temperature. Harshvardhan [45] found that the lapse rate in units of kelvin per kilometer from the SST to the cloud top can be well represented by Equation (1), which has been cited in many other studies when examining CTH in stratocumulus regions [46–48]. Therefore, this modification is used here to reduce potential errors in the CTH data:

$$\frac{SST - T_{top}}{CTH} = 9.2 \exp\left[-\left(\frac{CTH}{4.8}\right)^2\right],\tag{1}$$

where T_{top} is the actual CTT, and SST is the surface temperature in the ocean area filtered by the land-sea mask. The modified CTH is shown in Figure 2, and is about 100–200 m lower compared to the original.
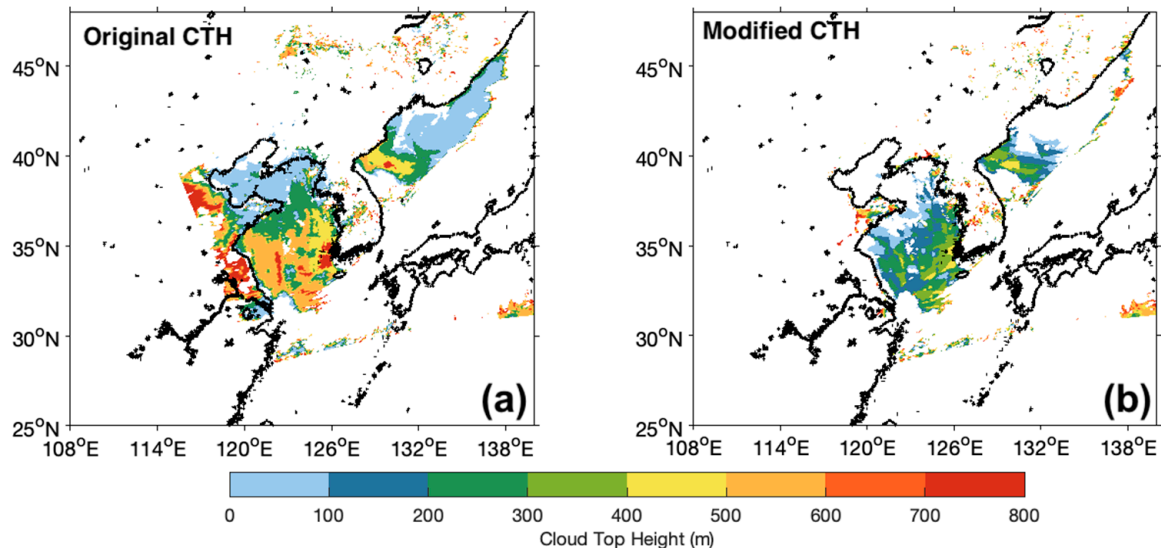

Figure 2. An example of CTH modification for the fog case was on 13 May 2018. (**a**) The original CTH of 5 km resolution from MODIS Aqua L2 cloud data product, (**b**) the modified CTH.

3.2. CTH Interpolation

The resolutions of the various products included in the MODIS dataset are different. For example, the resolution of CTH is 5 km, which is lower compared with DER, which has a resolution of 1 km. The GriddedInterpolant in MATLAB is used here to make all the data products the same resolution (1 × 1 km).

3.3. CTH Filtering

The temperature inversion height from the sounding files is used to estimate maximum fog thickness. Table 1 shows the temperature inversion heights of all 15 cases. The mean temperature inversion height is 633 m, and only 4 cases fall below the average. Therefore, the max value of the CTH is used as well, which falls between 700 and 800 m for all cases. Since clouds other than fog may be included in a particular satellite image, it is necessary to filter the data by CTH to limit the analysis to only pixels containing fog. To select the most appropriate CTH filtering threshold (e.g., max height for fog while eliminating non-fog clouds above the surface), CTH values of the mean temperature inversion height (633 m), 700 m, and 800 m are used for comparison. Figure 3 shows the CTH plot of a fog case on 13 May 2018, using different CTH threshold values. It shows that a CTH of 633 m (Figure 3b) results in the least complete fog area, with absent values in the middle and east areas (even though the fog is confirmed in those locations by visual inspection of RGB visible imagery, Figure 3a). The fog area is more complete when the maximum CTH is 700 m (Figure 3c), but the middle of the fog area is still empty. A CTH maximum value of 800 m includes all details of the fog area (Figure 3d). Also, we can see more intuitively from Table 1 that a CTH of 800 m has the most pixels. Therefore, the maximum CTH of 800 m is used when investigating the fog thickness in the rest of this work.
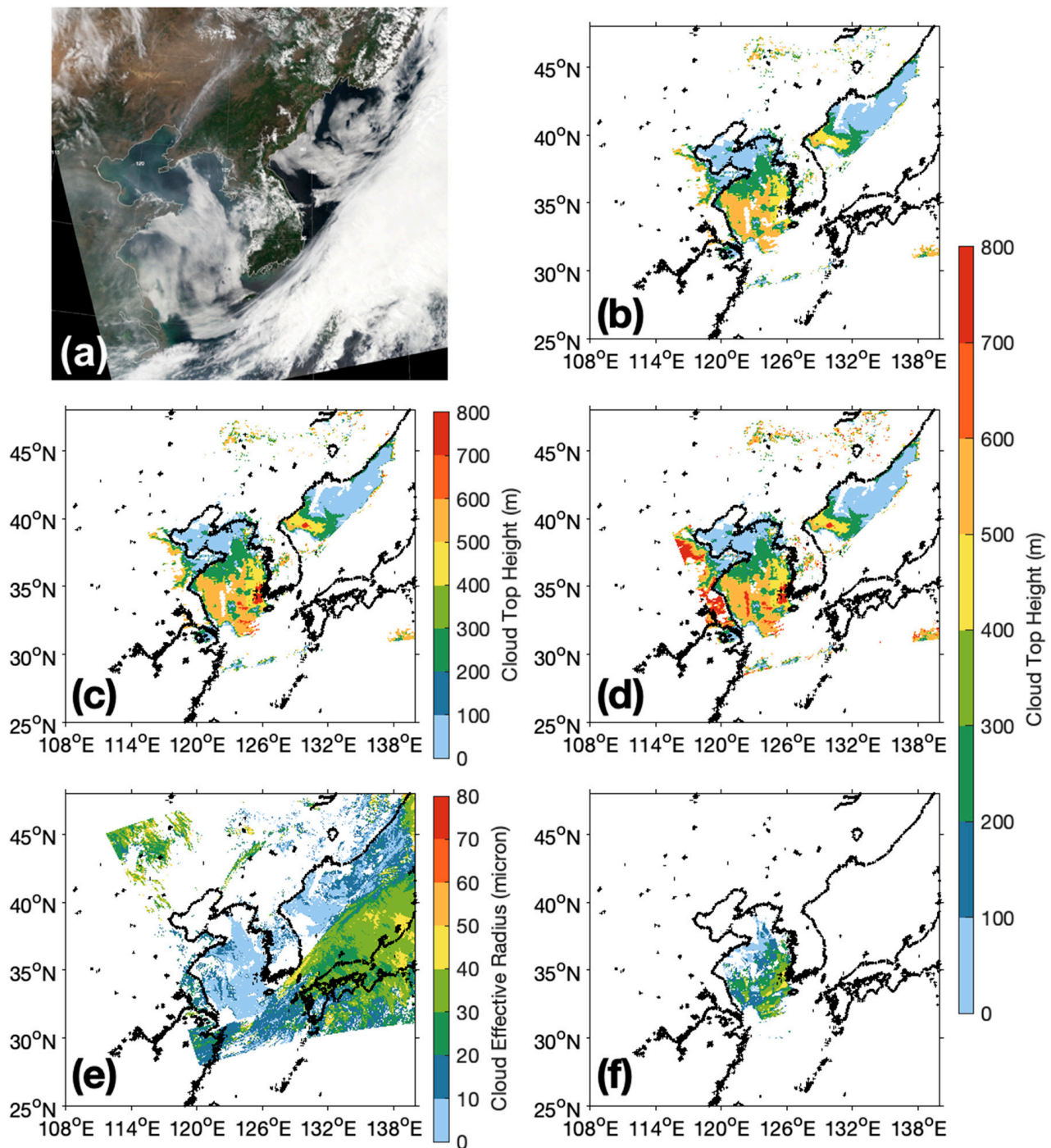
Figure 3. MODIS Aqua L1B Granule Image of a fog case on 13 May 2018 (**a**), and CTH of (**b**) mean temperature inversion height 633 m, (**c**) 700 m, (**d**) 800 m. (**e**) DER at 1 km resolution from MODIS Aqua L2 cloud data product, (**f**) result of the CTH for the selected fog area after applying the DER mask and land-sea mask.

Table 1. Yellow Sea fog cases. Granule means AOD, COT, DER, and SST values of the Yellow Sea area and mean temperature inversion height of QD station for the 15 selected sea fog cases.

Cases	Mean AOD	Mean Optical Thickness	Mean DER (Micron)	Mean SST (°C)	Temperature Inversion Height (m)	CTH Pixels (633 m)	CTH Pixels (700 m)	CTH Pixels (800 m)
4 May 2009	0.4605	9.7006	7.7972	10.6673	156	8680	13,696	13,907
14 April 2016	0.5102	9.3236	8.1057	7.9965	763	21,274	25,596	26,047
1 June 2011	0.5196	8.6431	8.4656	14.3343	Nan	5025	5508	6525
17 May 2011	0.5296	10.1061	7.7874	13.0364	754	19,072	21,151	22,377
6 June 2018	0.5488	8.0181	8.1329	15.8386	762	8281	8302	9554
3 May 2009	0.5596	7.569	8.464	10.137	166	4738	7491	7840
28 March 2012	0.5626	8.5409	8.4318	8.1441	211	20,746	24,841	25,140
9 April 2014	0.6189	10.4064	7.4462	8.0927	798	17,067	22,770	22,878
13 May 2018	0.7091	7.7615	7.6294	11.5593	732	24,247	25,345	27,705
2 May 2008	0.7559	7.3513	9.5294	13.2741	749	19,563	19,676	23,398
10 April 2016	0.7614	13.8427	8.2615	8.3672	759	16,448	20,348	20,525
8 April 2014	0.7639	8.4725	7.4141	9.2278	795	14,661	17,442	18,237
8 June 2007	0.907	8.4842	8.1693	16.8071	751	14,194	14,225	18,849
23 May 2006	0.9853	9.5122	8.4959	11.2939	756	15,834	20,376	21,435
13 April 2016	0.9905	9.1233	8.8142	8.9151	711	16,104	16,766	17,080

3.4. Fog Area Selection

For the fog case on 13 May 2018, the sea fog covers almost the entire Yellow Sea area, combined with the cloud in the south. There are some CTH values around Bohai Bay (Figure 3a), which can be identified as pollutants instead of sea fog according to the RGB satellite image. This means that CTH picks up not only fog and clouds but pollution as well. DER can exclude pollution, but it picks both fog and cloud information (Figure 3e). Therefore, when it comes to the selection of fog areas, both CTH and DER are used to identify and select fog pixels.

According to the result of the soundings, most of the fog cases have fog thicknesses around 800 m. By setting the maximum CTH as 800 m, upper-level clouds are excluded. This allows for the selection of the fog area in the Yellow Sea, while the non-fog cloud in the south can be filtered out. Combined with the DER plot, we can get rid of the pollution around Bohai Bay. In the end, by applying the land-sea mask and narrowing the latitude and longitude to the Yellow Sea area, the modified CTH of the whole fog area over the Yellow Sea fog can be selected without pollution and upper-level cloud contamination (Figure 3f).

4. Results

Bi-variate analyses between MODIS cloud properties are conducted to investigate the specific relationships between cloud properties. This analysis, combined with aerosol and SST observations from MODIS Aqua and GHRSST, shows that the formation of Yellow Sea fog is the result of both suitable synoptic and aerosol conditions.

4.1. Terrestrial Aerosol Type

MODIS Aqua L2 aerosol data are used to investigate terrestrial aerosol types around the Yellow Sea area. Figure 4 shows that sulfate and heavy absorbing smoke are the two main aerosol types around the Yellow Sea area. Out of the 15 selected cases, 12 cases have sulfate as the main aerosol type. Northeastern China is highly developed with numerous industrial and chemical complexes and cities, which produce sulfate pollution. The main terrestrial aerosol type for the other three cases is heavy absorbing smoke, combined with the sulfate and dust in the inland area, which is discussed separately below in Section 4.2.
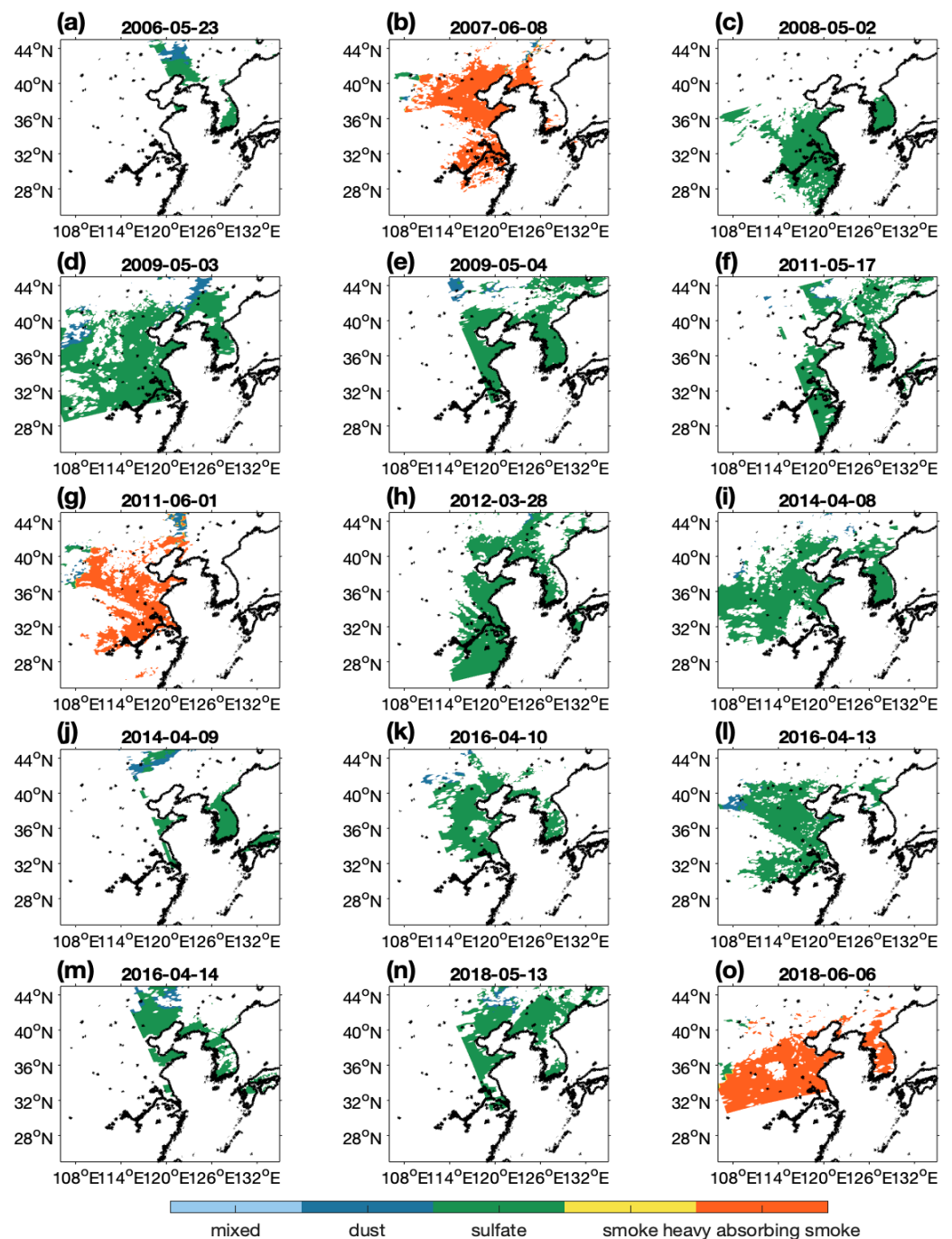
Figure 4. Terrestrial aerosol types surrounding the Yellow Sea region from the MODIS Aqua L2 aerosol data product. (**a**) Fog case on 23 May 2006, main aerosol type: sulfate and dust. (**b**) Fog case on 8 June 2007, main aerosol type: heavy absorbing smoke and sulfate. (**c**) Fog case on 2 May 2008, main aerosol type: sulfate. (**d**) Fog case on 3 May 2009, main aerosol type: sulfate and dust. (**e**) Fog case on 4 May 2009, main aerosol type: sulfate and dust. (**f**) Fog case on 17 May 2011, main aerosol type: sulfate. (**g**) Fog case on 1 June 2011, main aerosol type: heavy absorbing smoke, dust, and sulfate. (**h**) Fog case on 28 March 2012, main aerosol type: sulfate. (**i**) Fog case on 8 April 2014, main aerosol type: sulfate. (**j**) Fog case on 9 April 2014, main aerosol type: sulfate and dust. (**k**) Fog case on 10 April 2016, main aerosol type: sulfate and dust. (**l**) Fog case on 13 April 2016, main aerosol type: sulfate and dust. (**m**) Fog case on 14 April 2016, main aerosol type: sulfate and dust. (**n**) Fog case on 13 May 2018, main aerosol type: sulfate and dust. (**o**) Fog case on 6 June 2018, main aerosol type: heavy absorbing smoke and sulfate.

4.2. Fire Cases

Among all 15 fog cases, three of them have heavy absorbing smoke as the predominant terrestrial aerosol type. This heavy absorbing smoke was generated by fire activities across the Shandong Peninsula and is referred to hereafter as "fire cases" (8 June 2007; 1 June 2011; 6 June 2018).

The first fire case, on 8 June 2007, is shown in Figure 5. In this figure, fire occurrence is identified by thermal emissions (Figure 5d). Note that these data only show where fires occur, not how large (area burned) or how intense they are regarding smoke production or observed temperature. The density of fire occurrence in the south of the Shandong Peninsula corresponds with the pollutant band (red box) and higher aerosol concentration in the middle of the fog area (Figure 5a,m). Note that AOD data in the south are absent due to the coverage of clouds. The wind speed in the Yellow Sea region is lower than in the surrounding area (Figure 5j), which could be one of the reasons that contribute to the high concentration of heavy absorbing smoke around the Shandong Peninsula. Also, the weak southwesterly wind in the south Shandong Peninsula can transport the heavily absorbing smoke to the Yellow Sea region.

The second fire case was on 1 June 2011, located near the Shandong Peninsula (Figure 5e). The band of pollutants in the southwestern part of the fog area is also very clear in the visible RGB satellite imagery, corresponding to the higher AOD concentrations in the southern Yellow Sea region (Figure 5b,n). The wind speed in the Yellow Sea region is also lower than the surrounding area and from the southeast direction (Figure 5k), potentially transporting the heavy smoke to the Yellow Sea area.

The third heavy absorbing smoke case occurred on 6 June 2018. Thermal anomalies show separate groupings of fires in the south and west of the Shandong Peninsula (Figure 5f). However, no obvious pollution area can be identified from the MODIS visible RGB satellite image (Figure 5c) compared with the other two cases of thermal emissions indicative of fire activity. This is due to the strong southerly wind in the Shandong Peninsula (Figure 5l). The weak westerly and southwesterly winds that carry the aerosols from the fire locations encounter the stronger southerly wind and spread the heavy absorbing smoke to the Shandong Peninsula and Bohai Bay. A higher AOD can also be found around the Yellow Sea area which is 0.1895 larger than the sea fog case on 1 June 2011.

4.3. Relationship between Cloud Properties, Aerosols, and SST

SST plays an important part in the formation and maintenance mechanism of sea fog. Meanwhile, the presence of sea fog itself can also affect the chemical compositions of surrounding gaseous and aerosol pollutants [49]. For marine stratocumulus clouds, COT is found to be strongly correlated with the DER [50]. Meanwhile, a previous study shows that SST can affect cloud features by changing the cloud droplet number concentration [51]. Therefore, it is necessary to study the cloud properties, aerosols, and SST jointly.

The initial analysis completed here does not show strong correlations between the individual cloud properties and aerosols or SST for the selected 15 sea fog cases. High-resolution aerosol data co-located with the fog (cloud data) are not available for the data sources used in this study; therefore, a direct comparison between the two properties cannot be made. Therefore, the mean values of aerosol data of the Yellow Sea and cloud properties of the fog area are used to categorize and analyze the fog cases. Table 1 shows the mean values of the AOD, COT, DER, and SST values for the 15 selected cases. The cases are ranked according to the mean AOD values from lowest to highest. Ranking by other variables did not identify any clear patterns or relationships. The aerosol loading in this region is high, with many cases having similar values.

The scene mean values are not a high enough resolution to show any relationship between the mean AOD, COT, DER, and SST values, except for some differences caused by the synoptic conditions. For example, the difference in SST is mainly caused by seasonal variation. For the 15 selected cases, the earliest month when sea fog is observed is March, when the sea water is cooler compared with June due to the difference in solar radiation

intensity and duration. Therefore, to exclude the seasonal changes that influence our study, CTH, DER, and COT are selected to further study the relationship between cloud properties and aerosol concentrations. Here, we use a bi-variate comparison method to look at the variations between these three variables simultaneously. Three variables (x, y, and colormap) are utilized to show the interdependence of CTH, DER, and COT.
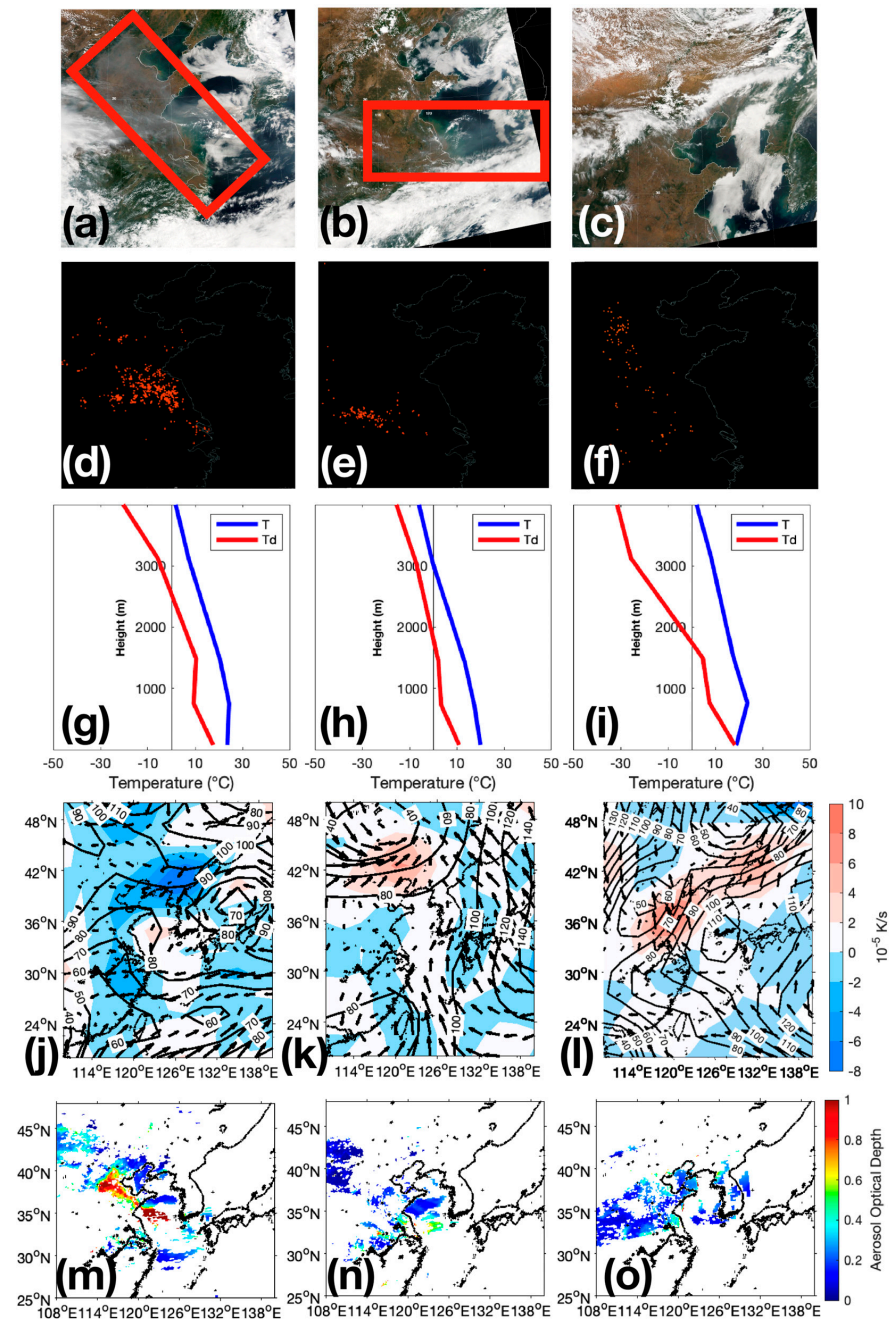

Figure 5. Fog cases with fire occurrences around the Shandong Peninsula on 8 June 2007 (the first column, (**a**,**d**,**g**,**j**,**m**)), 1 June 2011 (the second column (**b**,**e**,**h**,**k**,**n**)), and 6 June 2018 (the third column (**c**,**f**,**i**,**l**,**o**)). (**a**–**c**) Satellite RGB visible image from MODIS L2B Granule Image, red box: pollution band. (**d**–**f**) Thermal indicators of fire from NASA World View. (**g**–**i**) Vertical structures of air temperature (blue line) and dew point temperature (red line) from Sounding files at Qingdao Station. (**j**–**l**) Temperature advection calculated from the NECP/NCAR reanalysis data. The black line indicates the geopotential height at 1000 mb, the black arrows indicate the wind direction at the speed of 10 m/s unit, and the red (blue) areas indicate the warm (cold) temperature advection. (**m**–**o**) AOD from MODIS Aqua L2 aerosol data product.

4.4. Bi-Variate Comparison

Different combinations of these three parameters (CTH, DER, and COT) were tried when doing the bi-variate comparison with CTH as the *y*-axis, DER as the *x*-axis, and COT as the colormap providing identifiable and physically justifiable patterns. Figure 6 shows the result of the bi-variate comparison for all 15 cases. The most common interdependence pattern observed using the bi-variate method is what will be referred to hereafter as the "Diagonal Pattern", with larger COT values in the upper left and lower values in the bottom right. The second pattern is deemed the "Left-Right Pattern", where larger COT values are identified on the left and lower values on the right. The third pattern, called the "Inverse-Diagonal Pattern", refers to the distribution with larger COT values in the upper right and lower values in the bottom left. Each of these three patterns will be discussed in the following sections.

4.4.1. Diagonal Pattern Cases

Among the 15 sea fog cases, 11 of them show the Diagonal Pattern (Figure 6a,d–j,l–n). In these cases, larger values of COT are related to smaller DER and higher CTH values. Pollution levels in the Yellow Sea area are higher than in the surrounding areas, resulting in a greater proportion of smaller droplets in fog, e.g., low DER [52]. The smaller fog droplets can result in a thicker fog and larger cloud optical thickness. The Diagonal Pattern is the most common pattern among all the sea fog cases identified in this work and is indicative of the first aerosol indirect effect, even though we cannot evaluate the impact of the AOD directly since we do not have simultaneous co-located aerosol and cloud data.

The fog case on 28 March 2012 is taken as an example to analyze the detailed information regarding the relationship between CTH, COT, and DER. Figure 7c–e illustrates these three variables from the bi-variate comparison separately. The droplet DER is smaller in the middle of the sea fog area, which corresponds to the larger CTH values and larger COT in that area (Figure 7a,c,d). For the southern part of the fog area, the DER values are larger, and the bigger droplets result in thinner fog, corresponding with smaller COT values in that area.

The main terrestrial aerosol type for the fog case on 28 March 2012 is sulfate (Figure 4), which is caused by general industrial emissions. There is a clear pollutant band in the middle of the fog area from the satellite image (Figure 1c, yellow box), which corresponds to the larger AOD values in that area (Figure 7a). This pollutant band can cause smaller fog droplets in the middle of the fog area and result in thicker fog in that area. The easterly wind is weak on this day (Figure 7b) and can explain the formation of this pollutant band over the Yellow Sea area.

4.4.2. Left-Right Pattern

Figure 6c,k shows two fog cases, on 2 May 2008 and 10 April 2016, with the Left-Right Pattern. We see a different relationship than we do with the Diagonal Pattern, such that a larger COT corresponds to a smaller DER but also a smaller CTH. In these cases, smaller fog droplets result in thinner fog, which is unexpected if the first aerosol indirect effect were occurring

Figure 8 shows the CTH plot of these two cases. For these two cases, the CTH values in most of the fog areas are below the mean temperature inversion height (633 m), even as low as 0 m. The extremely thin fog in these two cases results in large COT values concentrated at the bottom left corner where the CTH ranges from 0 to 200 m, therefore causing the Left-Right Pattern where the CTH is lower for smaller DER values when the COT is larger.
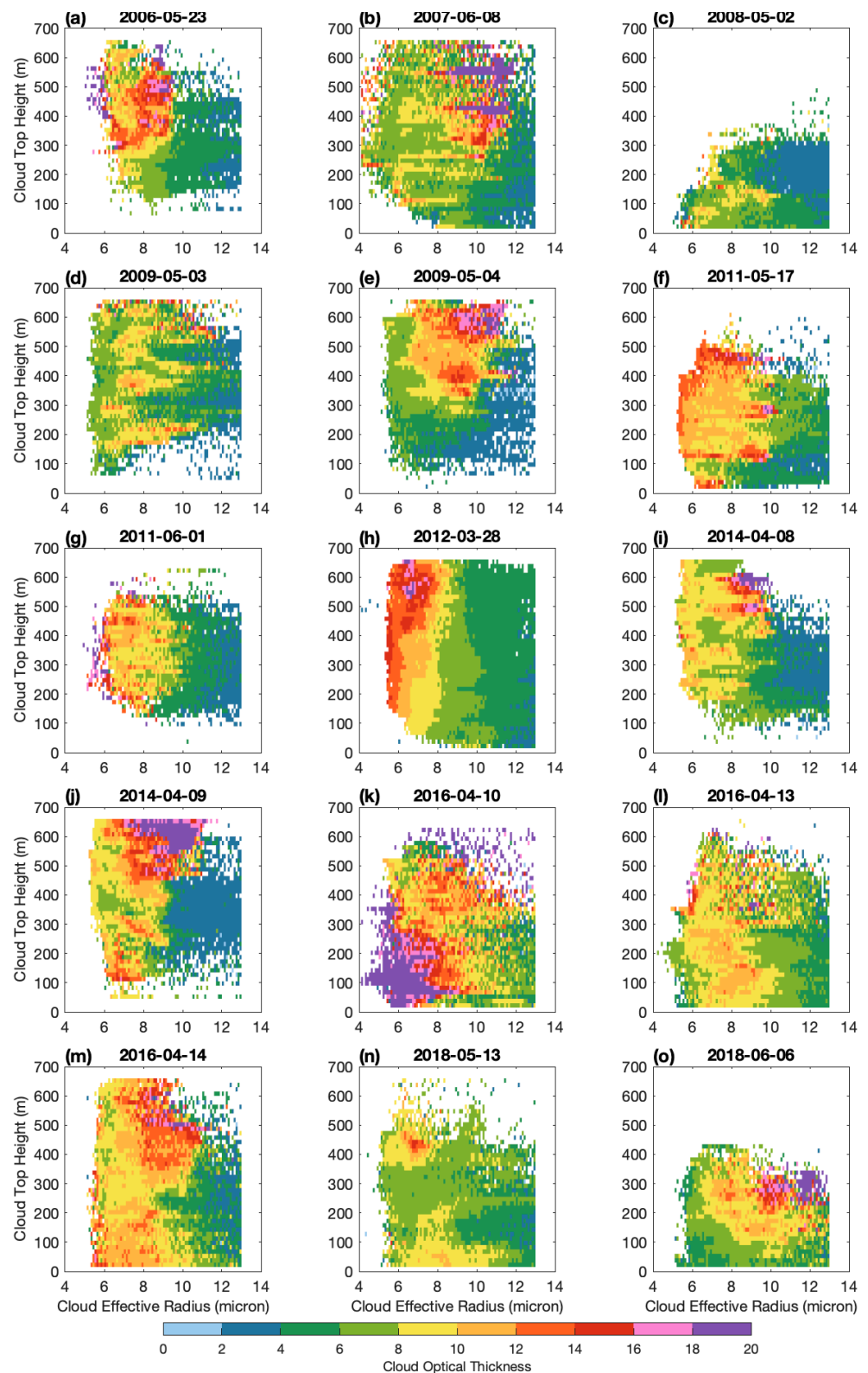
Figure 6. Bi-variate comparison for 15 fog cases. Diagonal Pattern (**a**,**d**–**j**,**l**–**n**) refers to distributions with larger COT values corresponding to smaller DER values and larger CTH values. Left-Right Pattern (**c**,**k**) refers to distributions with larger COT value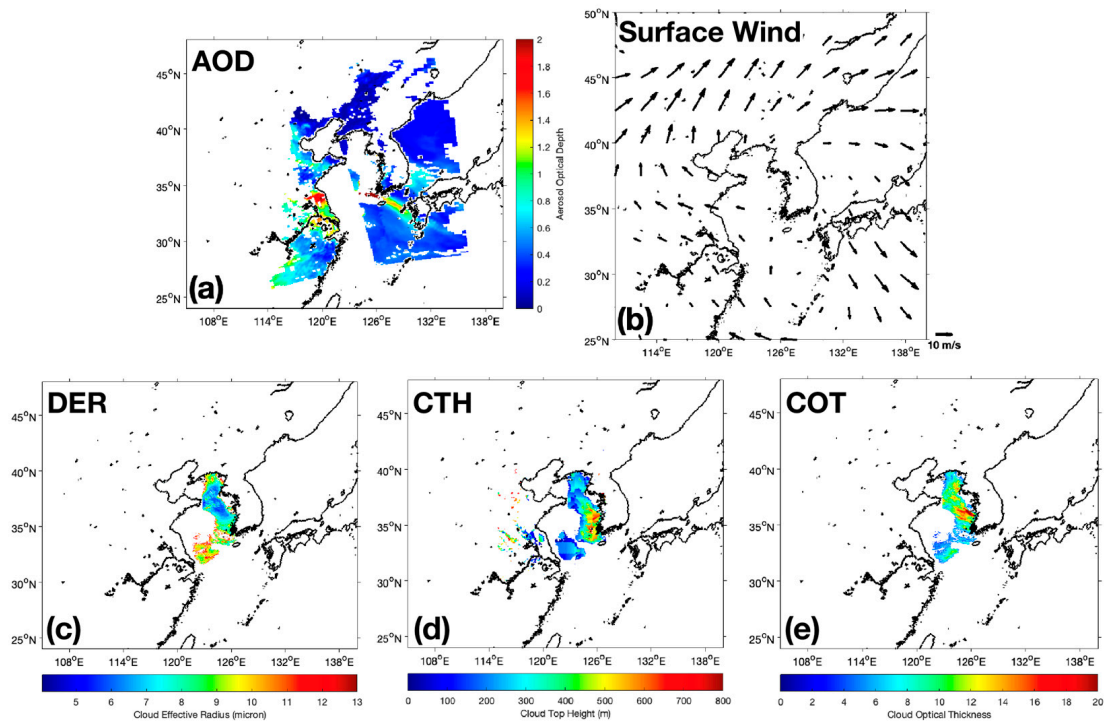s corresponding to larger DER values and smaller CTH values. Inverse-Diagonal Pattern (**b**,**o**) refers to distributions with larger COT values corresponding to both larger DER values and larger CTH values.

Figure 7. Aerosol, wind conditions, and cloud properties for the sea fog case on 28 March 2012, from MODIS Aqua L2 cloud data. (**a**) AOD form MODIS Aqua L2 aerosol data product. (**b**) Surface wind from NCEP/NCAR reanalysis dataset. (**c**) DER. (**d**) CTH. (**e**) COT.
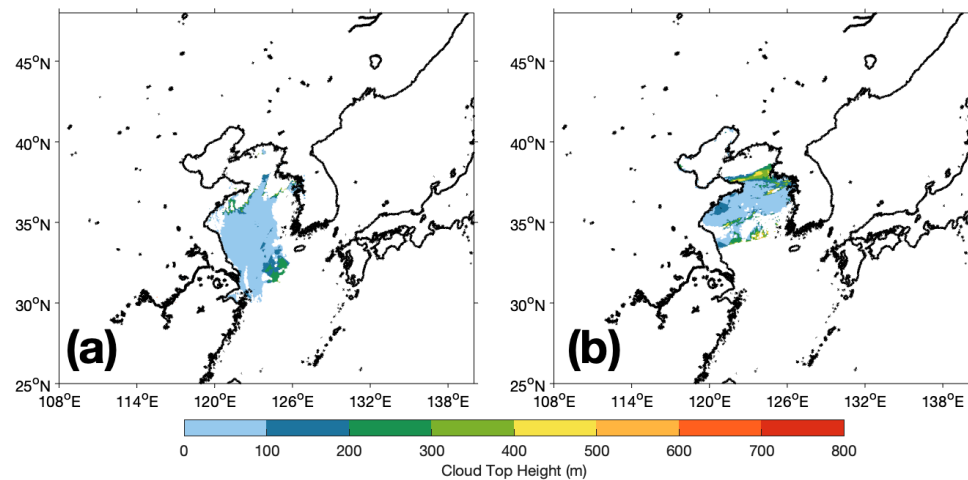

Figure 8. CTH from the MODIS Aqua L2 cloud data product. (**a**) Fog case on 2 May 2008. (**b**) Fog case on 10 April 2016.

4.4.3. Inverse Diagonal Pattern

Figure 6b,o shows the Inverse-Diagonal Pattern. In this situation, larger values of COT are correlated with both a larger DER and higher CTH.

As an example of the Inverse-Diagonal Pattern, Figure 9 shows the DER, CTH, and COT for the fog case on 8 June 2007. This case is also a "fire case", with fire locations in the south of the Shandong Peninsula. Due to the influence of active fires, there is a clear band of pollutants in the middle of the fog area in the visible satellite image, and the AOD value is higher over that area (Figure 5a,m). The fog area can be divided into two different parts by the pollutant band. In the north part, there is less pollution, and the DER is larger, while the southern part is more polluted, and the droplet DER values are smaller around the pollutant band.
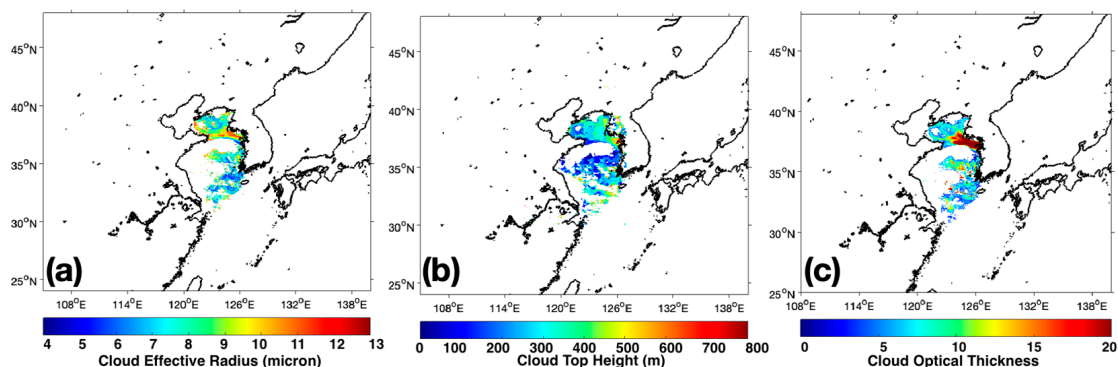
Figure 9. Cloud properties and aerosol for the sea fog case on 8 June 2007, from the MODIS Aqua L2 cloud data. (**a**) DER. (**b**) CTH. (**c**) COT.

Previous studies showed that the meteorological conditions that favor the sea fog process also favor the accumulation of aerosols and pollutants [21]. The droplet DER is smaller for fog compared with clouds, especially in polluted areas [52]. Observations have shown that droplet DER is negatively correlated with CTH [53]. This means that the smaller DER in the south part of the fog area (Figure 9a) would be expected to correspond with a larger CTH as well as a larger COT. However, both the CTH and COT are lower in that area (Figure 9b), the opposite of what we would expect due to the first aerosol indirect effect. Thus, this case suggests that the semi-direct effect is responsible for the observed relationship. In this fog case, the heavy absorbing smoke that is produced by the fires in the south of the Shandong Peninsula is potentially warming the air in the boundary layer and evaporating or reducing the fog over that area. This is a potential explanation for the fog being thinner near the main band of aerosols rather than thicker as observed in the more common Diagonal Pattern cases.

Among these three sea fog cases with confirmed fire occurrence around the Shandong Peninsula, two cases (8 June 2007 and 6 June 2018) show the Inverse-Diagonal Pattern while the fog case on 1 June 2011 does not. The opposite pattern exists for these three "fire cases" under the same aerosol type (heavy absorbing smoke) and pollution conditions, indicating that the synoptic aspects need to be considered. Figure 5g–i shows the vertical structure of the air temperature and dew point temperature for these three cases. From the soundings, the temperature inversion heights for both fog cases, 8 June 2007 and 6 June 2018, are around 700 m (Figure 5g,i). The dew point temperature and temperature are close near the surface, which indicates a moist boundary layer condition. However, there is no obvious temperature inversion for the fog case on 1 June 2011, and the boundary layer is dryer (Figure 5h).

Figure 5j–l shows the temperature advection for the three "fire cases." Both the fog cases, 8 June 2007 and 1 June 2011, show cold advection in the Shandong Peninsula (Figure 5j,k). For the fog case on 8 June 2007, there is weak warm advection in the Yellow Sea area with strong cold advection in the north of the Yellow Sea (Figure 5j), while only weak cold advection can be found in the west of the Yellow Sea area with warm advection in the north of Bohai Bay for the fog case on 1 June 2011 (Figure 5k). The fog case on 6 June 2018 (Figure 5l) shows strong warm advection in the Yellow Sea area, which corresponds with cold advection in the middle plain of China. By comparing these three cases, we can find that there is no strong temperature difference between the North and South Yellow Sea for the fog case on 1 June 2011.

The fog cases on both 1 June 2011 and 8 June 2007 show weak wind compared with the strong southerly wind in the fog case on 6 June 2018, which can transport the heavy absorbing smoke out of the Shandong Peninsula. However, the fog case on 1 June 2011 has the lowest mean AOD concentration over the Yellow Sea area (Table 1, 0.1895 lower than the sea fog case on June 6, 2018, 0.3847 smaller than the sea fog case on 8 June 2007).

Though there are fires identified around the Shandong Peninsula, the drier boundary condition and weak temperature advection combined with the lower AOD concentration are not sufficient to trigger the semi-direct effect for the fog case on 1 June 2011. Therefore, the bi-variate comparison of the fog case on 1 June 2011 shows the Diagonal Pattern while, for the other two "fire cases", the strong temperature difference, good moisture condition in the boundary layer, and sufficient aerosol combine to favor the formation of sea fog and create the appropriate conditions for the semi-direct effect to occur and contribute to the Inverse-Diagonal Pattern.

4.4.4. Sum Bi-Variate Comparison

Figure 10 shows a combined bi-variate comparison of all 15 fog cases. When looking at it in detail, we can find that some larger COT values in the bottom left corner are due to the zero values for the two cases of the Left-Right Pattern. The larger values of COT in the upper-middle are indicative of the semi-direct effect for these two "fire cases" with the Inverse-Diagonal Pattern. Overall, this figure shows a Diagonal Pattern with larger values of COT related to both a smaller DER and higher CTH in the dominant pattern in the Yellow Sea region.
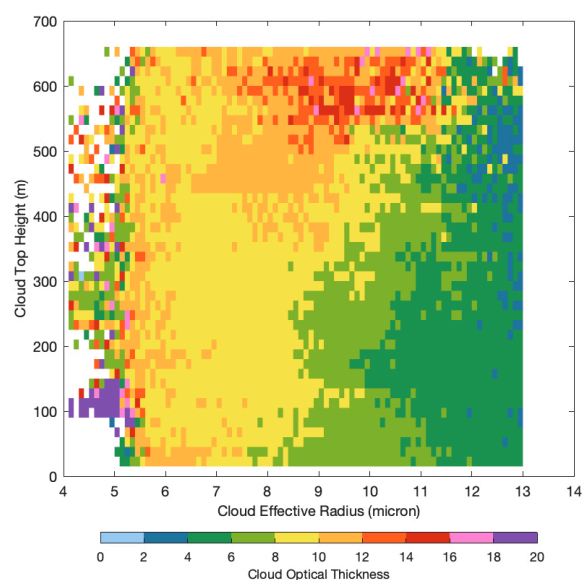

Figure 10. The sum bi-variate comparison of the 15 fog cases.

5. Conclusions

In this study, various datasets including surface observation stations, satellite data, and reanalysis models are used to investigate fog characteristics under different aerosol conditions for a total of 15 sea fog cases. Different from previous studies, this study utilizes high-resolution data from MODIS Aqua L2 to investigate the relationship between aerosols, cloud properties, and the SST. The high-resolution data provide a more detailed and holistic view of the Yellow Sea area of each event rather than a single point from a fixed surface observation station or a narrow slice from an aircraft. They show that satellite data can be an effective tool when investigating how pollution, which is increasing in the Yellow Sea region, will impact fog. The air pollution in the Yellow Sea region is complicated due to the heavy use of fossil fuels and human activities such as industrial and automotive/vehicular emissions, with sulfate and nitrate being the main secondary aerosol particles in Northern and Eastern China. This study shows evidence of two types of pollutants (sulfate and heavy absorbing smoke) and provides an in-depth investigation of the conditions of these cases.

Under the influences of seasonal variation, some variables such as the SST will change and cannot be used to study the relationship with other variables independently. Therefore, after careful selection, this study uses CTH, DER, and COT for the analysis. These

three variables are compared simultaneously to investigate the impact of the background aerosol type on cloud properties. This analysis does not show strong correlations between individual cloud properties and aerosols for the selected 15 sea fog cases due to the lack of coincident aerosol and cloud observations. Therefore, bi-variate comparison is used to comprehensively study the relationship between these variables. The results of the bi-variate comparison between CTH, DER, and COT indicate three distinct relationship patterns according to their differences in distribution. We term them the Diagonal Pattern, the Left-Right Pattern, and the Inverse Diagonal Pattern based on the observed patterns of COT concerning both the CTH and DER. Among all 15 cases, 11 cases show the Diagonal Pattern, with a larger COT on the upper left and a smaller COT on the bottom right. This means that larger values of COT are related to both a smaller DER and higher cloud height. Two cases show the Left-Right Pattern, which means that the larger COT values are related to smaller DER values but lower clouds. The CTH values of these two cases are lower compared with other cases, and the CTH values are even zero for some areas. The Inverse-Diagonal Pattern indicates that the larger COT values are related to both higher CTH and larger DER values. There are two cases of the Inverse-Diagonal Pattern, and both are "fire cases". Another "fire case" on 1 June 2011 shows a Diagonal Pattern. For this case, both the temperature inversion and temperature difference are weak compared with the other two "fire cases". These unfavorable synoptic conditions combined with insufficient aerosol amounts cannot trigger the semi-direct effect. The bi-variate comparison combined with the features of all 15 cases shows a Diagonal Pattern, though more cases are needed to better understand the observed relationships.

The results and conclusions in this study show the impacts of different aerosol conditions on the characteristics of sea fog, suggesting that further research on Yellow Sea fog and aerosol interactions is needed. Due to the limitations of current satellite remote sensing instruments, a better estimate of aerosol types and amounts over the yellow sea is needed to further study the aerosol conditions for Yellow Sea fog. In this study, the detection of Yellow Sea fog cases mainly relies on in situ and satellite observations. Uncertainties in our analysis are tied to the spatial and temporal resolutions of the data set and the uncertainties for the specific products used. MODIS Aqua L2 data have high special resolutions (down to 1 km), while the temporal resolution is relatively lower (5 min per Granule of L2 data). While sea fog can last for several hours, the possibility that the satellite passes over is low and will inevitably lead to some sea fog cases being missed. An additional impact on our analysis is due to the fact that the satellite imagery has an overhead view, which potentially includes other clouds at higher altitudes overhead. In addition, MODIS satellite data also have inherent uncertainties. The absolute uncertainty of the highest-quality data is approximately $(0.086 + 0.56\tau_M)/$AMF, where AMF stands for the geometric air mass factor [54]. The lack of vertical profile data from MODIS causes additional uncertainties because we need to rely on temperature and pressure information to determine cloud top/fog top height and cannot determine the vertical location of fog relative to aerosols. Synoptic conditions are another factor that influences the fog pattern over the Yellow Sea area and needs further investigation. This study briefly shows how the synoptic conditions can influence fog thickness for the highlighted "fire cases". This suggests that a deeper analysis of synoptic conditions for all cases has the potential to reveal further insight into fog formation and occurrence in the Yellow Sea. Evidence of the semi-direct effect on sea fog for three cases suggests this is another area for future research if more cases can be identified and analyzed. The granule mean of the SST for each fog event cannot intuitively show the role of SST in Yellow Sea fog events. Therefore, more research to study the relationship between the SST, aerosols, and cloud properties by using bi-variate comparison would be of value.

For future work, the relationship revealed by the bi-variate comparison may help with using aerosols to modulate fog evolution and contribute to improving sea fog simulation and prediction.

References

1. Baines, P.G. Sea fog. *Dyn. Atmos. Ocean.* **1987**, *11*, 92–93. [CrossRef]
2. Koračin, D.; Dorman, C.E.; Lewis, J.M.; Hudson, J.G.; Wilcox, E.M.; Torregrosa, A. Marine fog: A review. *Atmos. Res.* **2014**, *143*, 142–175. [CrossRef]
3. Koračin, D.; Dorman, C.E. (Eds.) *Marine Fog: Challenges and Advancements in Observations, Modeling, and Forecasting*; Springer International Publishing: Cham, Switzerland, 2017. [CrossRef]
4. Gultepe, I.; Tardif, R.; Michaelides, S.C.; Cermak, J.; Bott, A.; Bendix, J.; Müller, M.D.; Pagowski, M.; Hansen, B.; Ellrod, G.; et al. Fog Research: A Review of Past Achievements and Future Perspectives. *Pure Appl. Geophys.* **2007**, *164*, 1121–1159. [CrossRef]
5. Heo, K.-Y.; Ha, K.-J.; Mahrt, L.; Shim, J.-S. Comparison of advection and steam fogs: From direct observation over the sea. *Atmos. Res.* **2010**, *98*, 426–437. [CrossRef]
6. Zhang, S.-P.; Xie, S.-P.; Liu, Q.-Y.; Yang, Y.-Q.; Wang, X.-G.; Ren, Z.-P. Seasonal Variations of Yellow Sea Fog: Observations and Mechanisms. *J. Clim.* **2009**, *22*, 6758–6772. [CrossRef]
7. Yang, Y.; Hu, X.-M.; Gao, S.; Wang, Y. Sensitivity of WRF simulations with the YSU PBL scheme to the lowest model level height for a sea fog event over the Yellow Sea. *Atmos. Res.* **2019**, *215*, 253–267. [CrossRef]
8. Huang, M. Synoptic and climatic characteristics of Yellow Sea fog and causation analysis. *J. Trop. Meteorol./Redai Qixiang Xuebao* **2011**, *27*, 920–929.
9. Cho, Y.-K.; Kim, M.-O.; Kim, B.-C. Sea Fog around the Korean Peninsula. *J. Appl. Meteorol.* **2000**, *39*, 2473–2479. [CrossRef]
10. Jian, M.; Fangli, Q.; Changshui, X.; Yongzeng, Y. Tidal effects on temperature front in the Yellow Sea. *Chin. J. Oceanol. Limnol.* **2004**, *22*, 314–321. [CrossRef]
11. Zhang, S.; Li, M.; Meng, X.; Fu, G.; Ren, Z.; Gao, S. A Comparison Study Between Spring and Summer Fogs in the Yellow Sea-Observations and Mechanisms. *Pure Appl. Geophys.* **2012**, *169*, 1001–1017. [CrossRef]
12. Zhang, S.; Chen, Y.; Long, J.; Han, G. Interannual variability of sea fog frequency in the Northwestern Pacific in July. *Atmos. Res.* **2015**, *151*, 189–199. [CrossRef]
13. Rosenfeld, D. Aerosols, Clouds, and Climate. *Science* **2006**, *312*, 1323–1324. [CrossRef] [PubMed]
14. Twomey, S. The Influence of Pollution on the Shortwave Albedo of Clouds. *J. Atmos. Sci.* **1977**, *34*, 1149–1152. [CrossRef]
15. Albrecht, B.A. Aerosols, Cloud Microphysics, and Fractional Cloudiness. *Science* **1989**, *245*, 1227–1230. [CrossRef] [PubMed]
16. Houghton, J.T.; John, T. *Climate Change 2001: The Scientific Basis: Contribution of Working Group I to the Third Assessment Report of the Intergovernmental Panel on Climate Change*; Cambridge University Press: Cambridge, UK, 2001.
17. Lohmann, U.; Feichter, J. Global indirect aerosol effects: A review. *Atmos. Chem. Phys.* **2005**, *5*, 715–737. [CrossRef]
18. Myhre, G.; Myhre, C.E.L.; Samset, B.H.; Storelvmo, T. Aerosols and their Relation to Global Climate and Climate Sensitivity. *Nat. Educ. Knowl.* **2013**, *4*, 7.
19. Hansen, J.; Sato, M.; Ruedy, R. Radiative forcing and climate response. *J. Geophys. Res. Atmos.* **1997**, *102*, 6831–6864. [CrossRef]
20. Ackerman, A.S.; Toon, O.B.; Stevens, D.E.; Heymsfield, A.J.; Ramanathan, V.; Welton, E.J. Reduction of Tropical Cloudiness by Soot. *Science* **2000**, *288*, 1042–1047. [CrossRef] [PubMed]
21. Jia, X.; Quan, J.; Zheng, Z.; Liu, X.; Liu, Q.; He, H.; Liu, Y. Impacts of Anthropogenic Aerosols on Fog in North China Plain. *J. Geophys. Res. Atmos.* **2019**, *124*, 252–265. [CrossRef]
22. Li, Z.; Guo, J.; Ding, A.; Liao, H.; Liu, J.; Sun, Y.; Wang, T.; Xue, H.; Zhang, H.; Zhu, B. Aerosol and boundary-layer interactions and impact on air quality. *Natl. Sci. Rev.* **2017**, *4*, 810–833. [CrossRef]
23. Sasakawa, M.; Uematsu, M. Chemical composition of aerosol, sea fog, and rainwater in the marine boundary layer of the northwestern North Pacific and its marginal seas. *J. Geophys. Res. Atmos.* **2002**, *107*, ACH 17-1–ACH 17-9. [CrossRef]
24. Beiderwieden, E.; Wrzesinsky, T.; Klemm, O. Chemical characterization of fog and rain water collected at the eastern Andes cordillera. *Hydrol. Earth Syst. Sci.* **2005**, *9*, 185–191. [CrossRef]
25. Pant, V.; Deshpande, C.G.; Kamra, A.K. Changes in concentration and size distribution of aerosols during fog over the south Indian Ocean. *J. Earth Syst. Sci.* **2010**, *119*, 479–487. [CrossRef]

26. Mazoyer, M.; Burnet, F.; Denjean, C.; Roberts, G.C.; Haeffelin, M.; Dupont, J.-C.; Elias, T. Experimental study of the aerosol impact on fog microphysics. *Atmos. Chem. Phys.* **2019**, *19*, 4323–4344. [CrossRef]

27. Wei, J.; Jin, Q.; Yang, Z.; Zhou, L. Land–atmosphere–aerosol coupling in North China during 2000–2013. *Int. J. Climatol.* **2017**, *37*, 1297–1306. [CrossRef]

28. Wang, X.; Chen, J.; Sun, J.; Li, W.; Yang, L.; Wen, L.; Wang, W.; Wang, X.; Collett, J.L.; Shi, Y.; et al. Severe haze episodes and seriously polluted fog water in Ji'nan, China. *Sci. Total Environ.* **2014**, *493*, 133–137. [CrossRef] [PubMed]

29. Tao, M.; Wang, L.; Chen, L.; Wang, Z.; Tao, J. Reversal of Aerosol Properties in Eastern China with Rapid Decline of Anthropogenic Emissions. *Remote Sens.* **2020**, *12*, 523. [CrossRef]

30. Jia, X.; Guo, X. Impacts of Secondary Aerosols on a Persistent Fog Event in Northern China. *Atmos. Ocean. Sci. Lett.* **2012**, *5*, 401–407. [CrossRef]

31. Kroll, J.H.; Seinfeld, J.H. Chemistry of secondary organic aerosol: Formation and evolution of low-volatility organics in the atmosphere. *Atmos. Environ.* **2008**, *42*, 3593–3624. [CrossRef]

32. Kaul, D.S.; Gupta, T.; Tripathi, S.N.; Tare, V.; Collett, J.L. Secondary Organic Aerosol: A Comparison between Foggy and Nonfoggy Days. *Environ. Sci. Technol.* **2011**, *45*, 7307–7313. [CrossRef]

33. Zuidema, P.; Redemann, J.; Haywood, J.; Wood, R.; Piketh, S.; Hipondoka, M.; Formenti, P. Smoke and Clouds above the Southeast Atlantic: Upcoming Field Campaigns Probe Absorbing Aerosol's Impact on Climate. *Bull. Am. Meteorol. Soc.* **2016**, *97*, 1131–1135. [CrossRef]

34. Salomonson, V.V.; Barnes, W.; Masuoka, E.J. Introduction to MODIS and an Overview of Associated Activities. In *Earth Science Satellite Remote Sensing*; Qu, J.J., Gao, W., Kafatos, M., Murphy, R.E., Salomonson, V.V., Eds.; Springer: Berlin/Heidelberg, Germany, 2006; pp. 12–32. [CrossRef]

35. Bari, D.; Bergot, T.; El Khlifi, M. Local Meteorological and Large-Scale Weather Characteristics of Fog over the Grand Casablanca Region, Morocco. *J. Appl. Meteorol. Climatol.* **2016**, *55*, 1731–1745. [CrossRef]

36. Li, P.; Fu, G.; Lu, C. Large-Scale Environmental Influences on the Onset, Maintenance, and Dissipation of Six Sea Fog Cases over the Yellow Sea. *Pure Appl. Geophys.* **2012**, *169*, 983–1000. [CrossRef]

37. Wu, D.; Lu, B.; Zhang, T.; Yan, F. A method of detecting sea fogs using CALIOP data and its application to improve MODIS-based sea fog detection. *J. Quant. Spectrosc. Radiat. Transf.* **2015**, *153*, 88–94. [CrossRef]

38. Yuan, Y.; Qiu, Z.; Sun, D.; Wang, S.; Yue, X. Daytime sea fog retrieval based on GOCI data: A case study over the Yellow Sea. *Opt. Express* **2016**, *24*, 787. [CrossRef]

39. MODIS Atmosphere Science Team. *MOD04_L2 MODIS/Terra Aerosol 5-Min L2 Swath 10 km [Dataset]*; NASA Level 1 and Atmosphere Archive and Distribution System Distributed Active Archive Center: Washington, DC, USA, 2015. [CrossRef]

40. Platnick, S.; Ackerman, S.A.; King, M.D.; Meyer, K.; Menzel, W.P.; Holz, R.E.; Baum, B.A.; Yang, P. *MODIS Atmosphere L2 Cloud Product (06_L2), NASA MODIS Adaptive Processing System*; Goddard Space Flight Center: Greenbelt, MD, USA, 2015.

41. Hao, Y.; Cui, T.; Singh, V.P.; Zhang, J.; Yu, R.; Zhang, Z. Validation of MODIS Sea Surface Temperature Product in the Coastal Waters of the Yellow Sea. *IEEE J. Sel. Top. Appl. Earth Obs. Remote Sens.* **2017**, *10*, 1667–1680. [CrossRef]

42. Atmospheric Soundings. Available online: http://weather.uwyo.edu/upperair/sounding.html (accessed on 1 June 2023).

43. Garay, M.J.; De Szoeke, S.P.; Moroney, C.M. Comparison of marine stratocumulus cloud top heights in the southeastern Pacific retrieved from satellites with coincident ship-based observations. *J. Geophys. Res. Atmos.* **2008**, *113*, 2008JD009975. [CrossRef]

44. Holz, R.E.; Ackerman, S.A.; Nagle, F.W.; Frey, R.; Dutcher, S.; Kuehn, R.E.; Vaughan, M.A.; Baum, B. Global Moderate Resolution Imaging Spectroradiometer (MODIS) cloud detection and height evaluation using CALIOP. *J. Geophys. Res. Atmos.* **2008**, *113*, 2008JD009837. [CrossRef]

45. Harshvardhan Guangyu Zhao Di Girolamo, L.; Green, R.N. Satellite-Observed Location of Stratocumulus Cloud-Top Heights in the Presence of Strong Inversions. *IEEE Trans. Geosci. Remote Sens.* **2009**, *47*, 1421–1428. [CrossRef]

46. Zuidema, P.; Painemal, D.; De Szoeke, S.; Fairall, C. Stratocumulus Cloud-Top Height Estimates and Their Climatic Implications. *J. Clim.* **2009**, *22*, 4652–4666. [CrossRef]

47. Painemal, D.; Zuidema, P. Assessment of MODIS cloud effective radius and optical thickness retrievals over the Southeast Pacific with VOCALS-REx in situ measurements: MODIS VALIDATION DURING VOCALS-REx. *J. Geophys. Res. Atmos.* **2011**, *116*, D24. [CrossRef]

48. Costantino, L.; Bréon, F.-M. Aerosol indirect effect on warm clouds over South-East Atlantic, from co-located MODIS and CALIPSO observations. *Atmos. Chem. Phys.* **2013**, *13*, 69–88. [CrossRef]

49. Jung, J.; Choi, Y.; Wong, D.C.; Nelson, D.; Lee, S. Role of Sea Fog Over the Yellow Sea on Air Quality with the Direct Effect of Aerosols. *J. Geophys. Res. Atmos.* **2021**, *126*, e2020JD033498. [CrossRef] [PubMed]

50. Szczodrak, M.; Austin, P.H.; Krummel, P.B. Variability of Optical Depth and Effective Radius in Marine Stratocumulus Clouds. *J. Atmos. Sci.* **2001**, *58*, 2912–2926. [CrossRef]

51. Zhou, X.; Zhang, J.; Feingold, G. On the Importance of Sea Surface Temperature for Aerosol-Induced Brightening of Marine Clouds and Implications for Cloud Feedback in a Future Warmer Climate. *Geophys. Res. Lett.* **2021**, *48*, e2021GL095896. [CrossRef]

52. Gultepe, I.; Pearson, G.; Milbrandt, J.A.; Hansen, B.; Platnick, S.; Taylor, P.; Gordon, M.; Oakley, J.P.; Cober, S.G. The Fog Remote Sensing and Modeling Field Project. *Bull. Am. Meteorol. Soc.* **2009**, *90*, 341–360. [CrossRef]

53. Suzuki, S.; Seto, S.; Oki, T. Relationship between cloud droplet effective radius and cloud top height for deep convective clouds in CloudSat data product. In Proceedings of the 2011 IEEE International Geoscience and Remote Sensing Symposium, Vancouver, BC, Canada, 24–29 July 2011; pp. 2649–2652. [CrossRef]
54. Sayer, A.M.; Hsu, N.C.; Bettenhausen, C.; Jeong, M.-J. Validation and uncertainty estimates for MODIS Collection 6 "Deep Blue" aerosol data. *J. Geophys. Res. Atmos.* **2013**, *118*, 7864–7872. [CrossRef]